AIAA JOURNAL
Vol. 39, No. 11, November 2001

Inflow Conditions in Stochastic Eulerian–Lagrangian Calculations of Two-Phase Turbulent Flow

Jinn-Cherng Yang* and Keh-Chin Chang†
National Cheng-Kung University, Tainan 701, Taiwan, Republic of China

The importance of the inlet conditions of the dispersed-phase fluctuating velocity on the analysis associated with the stochastic Lagrangian method, which is commonly used in the simulation of two-phase turbulent flows, is demonstrated through two well-defined problems. One is under the inlet condition of the carrier-phase turbulent kinetic energy k_g larger than the dispersed-phase turbulent kinetic energy k_p. The other is associated with $k_g < k_p$. A solution procedure accounting for the inlet conditions of the fluctuating dispersed-phase velocities in the stochastic Lagrangian calculation is developed. It is also concluded that the unsteady drag coefficient has to be considered in the model formulation when the condition of the Stokes number larger than $\mathcal{O}(10^1)$ is encountered in the examined two-phase turbulent flowfield.

Nomenclature

C_D	=	drag coefficient
D	=	orifice diameter, 0.64 mm
d_p	=	droplet diameter
g	=	gravity
K	=	history-force kernel
k	=	turbulent kinetic energy
n	=	number density, number of droplets per cubic meter
P, Q	=	value of probability density function
Re_p	=	droplet Reynolds number
r	=	radial coordinate
St	=	Stokes number, τ_p/τ_r
t	=	time
t_M	=	dimensionless time defined by Eq. (14)
U, u	=	instantaneous and mean velocities, respectively
$\boldsymbol{U}$	=	vector form of instantaneous velocity
x	=	axial or streamwise coordinate
y	=	transverse coordinate
α_{12}	=	ratio of velocity slips in two neighboring grid cells
Δt	=	time increment
ΔU	=	velocity slip, $U_g - U_p$
μ	=	viscosity
ρ	=	density
τ_p, τ_r	=	dynamic relaxation time and residence time of droplet, respectively
ϕ	=	factor accounting for deviation from the Stokesian drag

Subscripts

g	=	carrier phase
i	=	ith component
in	=	inlet
old	=	value at the preceding time step
p	=	dispersed phase
s	=	Stokesian drag
1, 2	=	upstream and downstream, respectively

Superscripts

$'$	=	fluctuation
$\bar{}$	=	ensemble averaging value defined by Eq. (19)

Received 23 May 2000; revision received 21 May 2001; accepted for publication 24 May 2001.

*Graduate Student, Department of Aeronautics and Astronautics.
†Professor, Department of Aeronautics and Astronautics; kcchang@mail.ncku.edu.tw. Senior Member AIAA.

I. Introduction

In the practical engineering simulation of dilute two-phase flows such as sprays, pneumatic transport of particles, cyclones, etc., a commonly used approach is the combined Eulerian–Lagrangian method, which treats the carrier phase (fluid) as a continuum and the dispersed phases (particles or droplets) as discrete entities. The carrier-phase transport equations are formulated in the Eulerian framework, and droplets (or particles, per se) are tracked along the Lagrangian trajectories in the carrier fluid as a result of forces acting on the droplets. Turbulent dispersion of the droplets in the carrier fluid are usually simulated by use of the stochastic (Monte Carlo) approach, which was originally developed by Gosman and Ioannides,[1] herein referred to as the conventional stochastic Eulerian–Lagrangian method. Recent comprehensive reviews on the conventional stochastic Eulerian–Lagrangian method can be found in Refs. 2–4. In the conventional stochastic Eulerian–Lagrangian method, which is also called the stochastic discrete-delta function method by Chen and Pereira,[5] the mean dispersed-phase properties at a grid node are determined using ensemble averaging of the properties of many individual droplets, in which their trajectories fall within the grid cell. Therefore, tracking a great number of trajectories is required to attain a statistically invariant solution.[5,6]

Dutta et al.[7] proposed a discrete probability function method for turbulent dispersion computation of the droplets that is capable of providing accurate simulation with low statistical noise. However, the need for a great number of computational droplets makes the method of Dutta et al.[7] more expensive than the conventional stochastic Lagrangian method. To improve the computational efficiency of the conventional stochastic Lagrangian method, Chen and Pereira[5] proposed a stochastic-probabilistic dispersion model, which was shown to be able to reduce the number of droplet trajectories to be tracked in the calculations.[5,8] The model proposed by Chen and Pereira[5] differs from the conventional stochastic one in that it solves additionally the spatial distributions of droplets along their trajectories. The information of these spatial distributions of droplets are, then, taken into account in the ensemble-averaging calculations of the dispersed-phase properties.

All of the stochastic Lagrangian models assume that the discrete entities (droplets or particles), moving in a turbulent carrier fluid, constantly encounter a series of energetic eddies randomly sampled from the carrier-phase flowfield. Chang and Yang[9] and Chang et al.[10] found that the use of an unsteady drag coefficient in modeling two-phase turbulent flows with the stochastic Lagrangian models is usually necessary to obtain correct information of the dispersed-phase turbulence characteristics. In addition, remarkable underpredictions of the partial turbulent kinetic energy, $(\overline{u_p'^2} + \overline{v_p'^2})/2$, of droplets were observed in the upstream flow regions, as compared to the measured data of Liu,[11] even in the calculation using the unsteady drag coefficient.[9] Moreover, the level of underprediction becomes more

remarkable as the droplet size is increased (see Fig. 8 in Ref. 9). The errors in predicting the partial turbulent kinetic energy of droplets were speculated from the neglect of the inlet fluctuating information for droplet velocities in the calculation, which is elaborated on hereafter.

All of the stochastic Lagrangian models adopt the stochastic operation that deals with the Lagrangian equation of instantaneous motion described as

$$\frac{\mathrm{d}U_{pi}}{\mathrm{d}t} = \frac{U_{gi} - U_{pi}}{\tau_p} + g_i \tag{1}$$

where the droplet dynamic relaxation time, which denotes a characteristic time of the droplet reaching its dynamic equilibrium with the carrier fluid, is defined by

$$\tau_p = \frac{4d_p\rho_p}{3C_D\rho_g|\Delta \boldsymbol{U}_g|} \tag{2}$$

and the instantaneous velocity of the carrier fluid is given by

$$U_{gi} = u_{gi} + u'_{gi} \tag{3}$$

where u'_{gi} is randomly determined from the random number generator in the computational process.

Equation (1) can be solved by iteratively integrating this nonlinear ordinary differential equation to an acceptable tolerance in a given time step, that is,

$$U_{pi} = U_{gi} - [U_{gi} - (U_{pi})_{\mathrm{old}}]\exp(-\Delta t/\tau_p) + g_i\tau_p[1 - \exp(-\Delta t/\tau_p)] \tag{4}$$

where the subscript old denotes the value at the beginning of the time increment Δt. Note the first time step as a droplet just leaves its inlet position. $(U_{pi})_{\mathrm{old}}$ now represents the instantaneous droplet velocity at the inlet. Nevertheless, to the best of our knowledge, most studies using the stochastic Eulerian–Lagrangian method, including our previous work,[9] did not consider the inlet u'_{pi} information in their calculations. Instead, only the mean quantities of droplet velocities, which were determined either from the measured data or from the assumed inlet profiles, were used in the calculations. Thus, Eq. (4) becomes

$$U_{pi} = U_{gi} - [U_{gi} - (u_{pi})_{\mathrm{in}}]\exp(-\Delta t/\tau_p) + g_i\tau_p[1 - \exp(-\Delta t/\tau_p)] \tag{5}$$

at the first integrating time step. Apparently, the use of Eq. (5) may introduce some errors in the downstream U_{pi} predictions, such as those shown in Fig. 8 of our previous work,[9] because one important turbulent characteristic of the dispersed phase, that is, the turbulent fluctuations of the droplet velocities, at the inlet is not considered in the calculation.

A rigorous theoretical analysis for a two-phase turbulent flow has to take into consideration the inlet turbulent characteristics of both phases. The stochastic Eulerian–Lagrangian method is theoretically capable of yielding a complete solution of both the carrier and dispersed phases, including mean and fluctuating quantities. Nevertheless, researchers commonly neglect of inlet u'_{pi} conditions in solving the equation of motion, such as that described in Eq. (5). Our preceding study[9] revealed that remarkable underpredictions of the partial kinetic energy for the large droplets in the upstream flow regions of a two-phase mixing layer might stem from the neglect of the inlet u'_{pi} conditions in the calculations. It is worthwhile to check how neglect of the inlet u'_{pi} conditions affects the complete solutions of the two-phase flows. The object of this work is, then, to develop an appropriate way of taking the inlet u'_{pi} conditions into account in the solution procedure of the analysis. Evaluation of the influences of the inlet u'_{pi} conditions on the prediction of two-phase turbulent flow is made through two representative, well-defined problems. One is associated with the inlet condition of $k_g > k_p$ and the other with $k_g < k_p$. Here, the turbulent kinetic energy of dispersed phase is defined by

$$k_p = \frac{1}{2}\sum_{i=1}^{3}\overline{u'^2_{pi}} \tag{6}$$

II. Test Problems

The experimental work of a droplet loading, planar mixing-layer flow in a vertical tunnel,[11,12] which is schematically shown in Fig. 1a, serves as the first test problem. The tunnel with a 150×150 mm^2 cross-sectional area at the test section was equally divided into two separate flow paths by an upstream central splitting plate. The mean velocities of the high- and low-speed streams were equal to 10.2 and 2.36 m/s, respectively. A Sono-Tek ultrasonic nozzle, located 800 mm upstream of the test section in the high-speed stream, generated polydispersed water droplets with the Sauter mean diameter of 54 μm. The trailing edge of the splitting plate was extended 150 mm into the test section. A rectangular coordinate was selected such that the streamwise x coordinate is downward with the origin at the central separation point of the splitting plate, and the transverse y coordinate is positive toward the high-speed stream side.

The second test problem is the experimental work of a hollow-cone spray[13,14] shown schematically in Fig. 1b. The spray nozzle was a pressure atomizer with an orifice diameter of 0.64 mm from which the water spray was injected vertically downward with a flow rate of 1.19 g/s at an injection pressure of 928 kPa (134.7 psi). The nominal cone angle was 80 deg. The exhaust system of the test stand provided a uniform curtain flow of surrounding air with a velocity of 0.5 m/s in the test section to avoid flow reversal. The test chamber cross section was 0.8×0.8 m with a length of 0.7 m. Because the spray is axisymmetric, a two-dimensional, cylindrical coordinate is selected so that the axial x coordinate (along the axis) is positive downward with the origin at the center of the atomizer exit and the radial r coordinate is positive away from the axis.

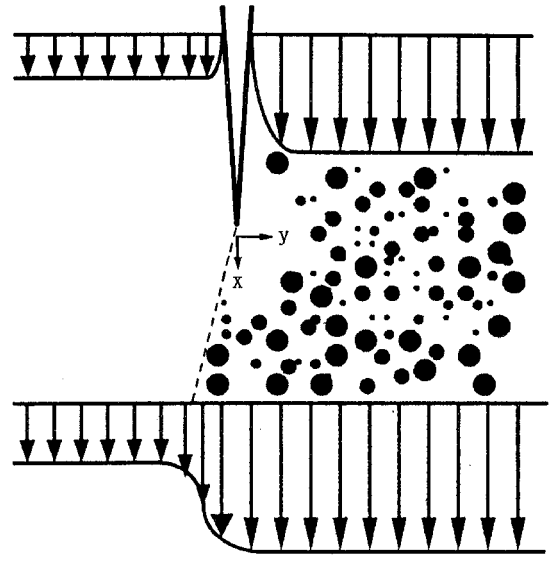

a) Planar mixing layer

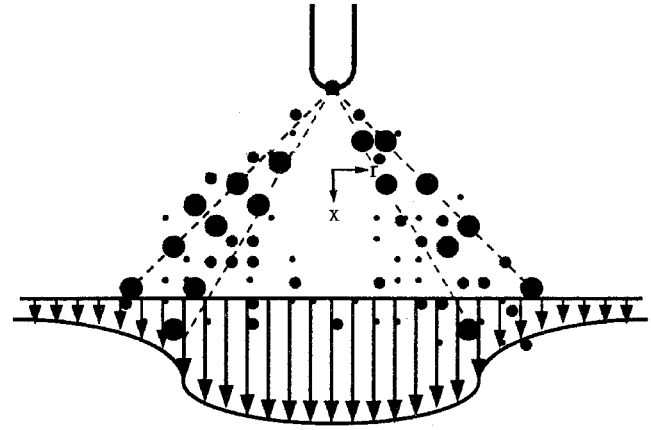

b) Hollow-cone spray

Fig. 1 Schematics of two-phase flowfields.

Measurements of the mean and fluctuating flow properties of both phases in these two experiments were made using a two-component phase Doppler particle analyzer (PDPA). A smoke generator (using kerosene as the working fluid) was used to generate seeding particles (nominal 2 μm) for the velocity measurements of the carrier fluid. The ensemble-averaged quantities were statistically calculated by collecting 30,000 valid sample data for each measurement point. Uncertainties in mean and fluctuating velocities of the carrier phase using the PDPA were within 2% in comparison with the measurements of a pitot tube measuring in the range from 1 to 10 m/s. The uncertainties of the measured dispersed-phase volume fluxes, by comparison with the metered liquid flow rate in the upstream water supply line, was less than 10% for the case of the two-phase mixing-layer flow and 20% for the case of the hollow-cone spray. Complete (three components of velocity) measurements at the streamwise/axial stations of $x = 5$ and 12.8 mm were made as the inlet conditions required for the theoretical analyses of the planar mixing-layer and hollow-cone spray, respectively.

The pressure hollow-cone atomizer generated a more dispersed size spectrum (2–150 μm) than the Sono-Tek ultrasonic nozzle (2–90 μm). Eight sets of data labeled with the (Sauter) mean droplet sizes of 10, 20, 30, 40, 50, 60, 70, and 80 μm were recorded in the experimental work on the planar mixing layer, and 10 data sets labeled with the (Sauter) mean droplet sizes of 7, 21, 35, 49, 63, 77, 91, 105, 119, and 133 μm were recorded in the experimental work on the hollow-cone spray. The configuration of the droplet loading, mixing layer problem, in which the droplets were issued at the far upstream position (0.95 m), lead to $k_g > k_p$ at the inlet position ($x = 5$ mm) as shown in Fig. 2a. This is the same as observed in most of the published experimental work on gas–particle flows such as that of Prevost et al.[15] In contrast, the hollow-cone spray problem, which is a practical spray in industrial applications, shows the opposite $k_p > k_g$ at the inlet station ($x/D = 20$) as seen in Fig. 2b. This is because the inlet position for this test problem is near the droplet injection (the atomizer) point, but located behind the region where the primary atomization process of the spray has been completed.[13]

III. Model Analysis

A. Physical Modeling

The configuration of the planar mixing-layer problem allows the use of the boundary-layer approximation, which neglects the diffusion terms along the streamwise direction, in the formulation of the carrier-phase governing equations. In contrast to the planar mixing-layer problem, the carrier-phase governing equations for the hollow-cone spray are two dimensionally elliptic due to the axisymmetric characteristic of the flowfield. The flowfields of these two test problems are determined through use of the k_g–ε_g model. The applicability of the k_g–ε_g model in the simulations of the two test problems has been demonstrated by Chang et al.[12,14] To account for the effects of turbulence modulation, the model originally proposed by Shuen et al.[16,17] and recently modified by Shang et al.[18] is used in the work. However, because the two-phase flow investigated in the mixing-layer problem is a very dilute case [typical dispersed-phase volumetric fraction of $\mathcal{O}(10^{-5})$], it was shown[12] that turbulence modulation effects could be ignored in modeling this test problem. In contrast, the typical dispersed-phase volumetric fraction in the hollow-cone spray was one order of magnitude higher than that in the mixing-layer flow. The consideration of the turbulence modulation effects in the modeling of the hollow-cone spray improved the flow predictions, but only to a slight extent.[14]

The dispersed phase is treated by tracking all individual entities when they move through the turbulence field of the carrier fluid. To account for the effects of the size spectra of the droplets, 8 and 10 discrete droplet sizes, which conform to the data sets recorded in the experiments, are used in the calculations of the droplet loading mixing layer and hollow-cone spray, respectively. For details of modeling these two problems, see Refs. 12 and 14.

An expression for the unsteady drag coefficient suggested in our previous work[9] is used in the calculations

$$C_D(t)/(C_D)_s = (1 - \alpha_{12})K(t) + \phi(Re_p), \qquad t > 0 \tag{7}$$

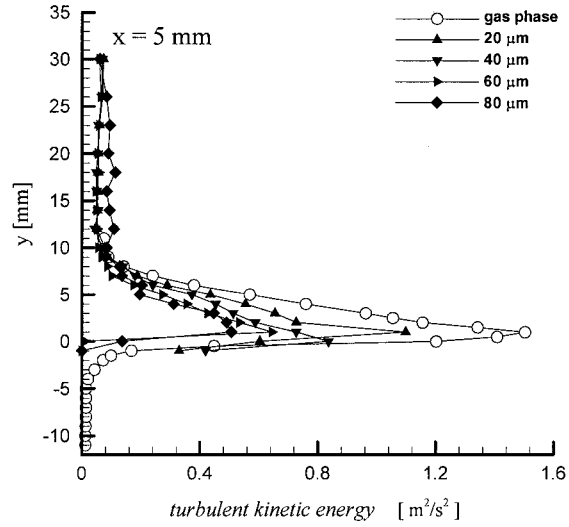

a) Two-phase mixing layer

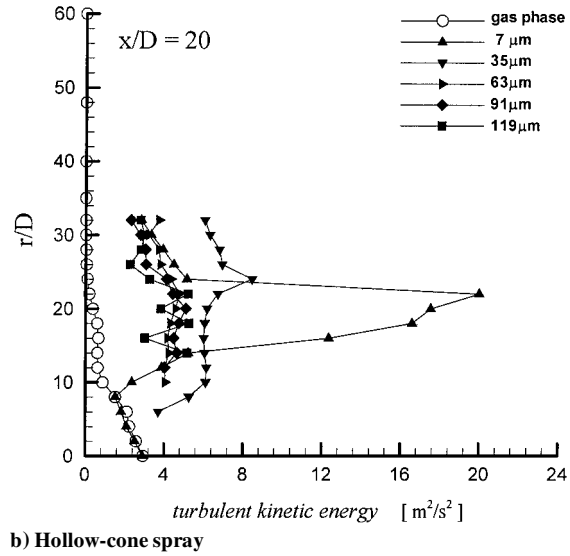

b) Hollow-cone spray

Fig. 2 Measured turbulent kinetic energy of carrier gas and droplets with several representative sizes at inlet positions.

where

$$\alpha_{12} = \Delta U_1/\Delta U_2 \tag{8}$$

$$Re_p = \rho_g|\Delta \boldsymbol{U}_g|d_p/\mu_g \tag{9}$$

The history-force kernel $K(t)$ is taken from the empirical one developed by Mei and Adrian[19]:

$$K(t) = \left\{\left(\frac{4\pi\mu_g}{\rho_g d_p^2}t\right)^{\frac{1}{4}} + \left(\frac{\pi\rho_g}{\mu_g d_p}\right)^{\frac{1}{2}} t\left[\frac{|\Delta \boldsymbol{U}_g|}{f_H(Re_p)}\right]^{\frac{3}{2}}\right\}^{-2} \tag{10}$$

with

$$f_H(Re_p) = 0.75 + 0.105Re_p \tag{11}$$

The factor $\phi(Re_p)$ of Eq. (7) accounts for deviation from the Stokesian drag coefficient, that is, $(C_D)_s = 24/Re_p$, at the steady state when the condition of $Re_p \ll 1$ is not met. One of the best correlations for $\phi(Re_p)$, compiled by Clift et al.,[20] is used:

$$\begin{aligned}
\phi(Re_p) &= 1 + (3/16)Re_p, && 0 < Re_p \le 0.01 \\
&= 1 + 0.1315Re_p^{(0.82 - 0.02171\ln Re_p)}, && 0.01 < Re_p \le 20 \\
&= 1 + 0.1935Re_p^{0.6305}, && 20 < Re_p \le 260
\end{aligned} \tag{12}$$

Note that the parameters affecting the value of $C_D(t)$ are not only α_{12} and Re_p but also d_p [see Eq. (10)]. Equation (7) returns to the identical form of the steady-state one for $t \gg 1$ because $K(t)$ asymptotically approaches zero value after a sufficiently long time.

For the special condition of $\alpha_{12} = 0$ (startup from rest) and $Re_p \leq 1$, Sano's analytical solution,[21] which is given hereafter, takes over the expression of $C_D(t)$ because its performance is better than that of Eq. (7):

$$\frac{C_D(t_M)}{(C_D)_s} = 1 + \frac{3}{16}Re_p\left\{\left[1 + \frac{16}{(Re_p t_M)^2}\right]\mathrm{erf}\left(\frac{1}{2}\sqrt{\frac{Re_p t_M}{2}}\right) + 2\sqrt{\frac{2}{\pi Re_p t_M}}\left(1 - \frac{4}{Re_p t_M}\right)\exp\left(-\frac{Re_p t_M}{8}\right)\right\} + \frac{9}{160}Re_p^2\,\ell n\left(\frac{1}{2}Re_p\right), \qquad t_M > 0 \tag{13}$$

with dimensionless time

$$t_M = 2|\Delta U_g|t/d_p \tag{14}$$

B. Numerical Solution Procedure

Calculation of the carrier-phase flowfield is performed with the finite volume method using the SIMPLER algorithm and the power law scheme.[22] The dispersed-phase equation of motion [Eq. (1)] is solved using the iterative integration as described in the first section.

To obtain statistically significant properties of the dispersed phase for a given discrete droplet size, an adequate number of computational droplets of the same discrete size, each corresponding to an instantaneous carrier-phase velocity as expressed in Eq. (3), has to be tracked in the stochastic Lagrangian method. For a given fluctuating velocity u'_{gi}, which is randomly sampled in the solution procedure at each integrating time step, there exists a corresponding value of the probability density function (PDF), that is, $P(u'_{gi})$. Because the measured U_{gi} histograms exhibited reasonably Gaussian distribution form,[10] these PDFs are represented using Gaussian functions, as defined hereafter, in the calculations:

$$P(u'_{gi}) = \frac{1}{\sqrt{2\pi}\sqrt{\overline{u'^2_{gi}}}}\exp\left[-\frac{1}{2}\left(\frac{u'_{gi}}{\sqrt{\overline{u'^2_{gi}}}}\right)^2\right] \tag{15}$$

The mean value of the droplet velocity at a specified grid cell was determined in past studies,[6,9,12,14] without accounting for the inlet u'_{pi} conditions, by the use of the ensemble-averaging concept, as follows:

$$u_{pi} = \frac{\sum_{m=1}^{M} n_m \cdot P[(u'_{gi})_m]\cdot(U_{pi})_m}{\sum_{m=1}^{M} n_m \cdot P[(u'_{gi})_m]} \tag{16}$$

where the index m is the mth computational droplet entering the control volume of a specified grid cell. The idea embedded in Eq. (15) is that because each U_{pi} is solved from Eq. (1) with a randomly given U_{gi}, it is necessary to account for the corresponding PDF value of U_{gi} as a weighting factor in the ensemble-averaging of Eq. (16). A similar concept can be applied to the calculation with consideration of the inlet u'_{pi} conditions as follows. Distributions of $(u'_{pi})_{\mathrm{in}}$ are made in the normalized Gaussian form of

$$Q[(u'_{pi})_{\mathrm{in}}] = \frac{1}{\sqrt{2\pi}\sqrt{\overline{(u'_{pi})^2_{\mathrm{in}}}}}\exp\left[-\frac{1}{2}\frac{(u'_{pi})^2_{\mathrm{in}}}{\overline{(u'_{pi})^2_{\mathrm{in}}}}\right] \tag{17}$$

which are good representations of the measured PDFs of u'_{pi}. (The typical shape of the u'_{pi} PDF can be seen in Figs. 4 and 5 of our previous work.[9]) The $(U_{pi})_{\mathrm{in}}$, which is required at the first integrating time step as in Eq. (4), is now constructed by the measured mean values $(u_{pi})_{\mathrm{in}}$ and a randomly sampled $(u'_{pi})_{\mathrm{in}}$. Thus, this computational droplet, which is issued from the lth position in the inlet section, is always associated with its corresponding PDF value to the inlet u'_{pi} information [for example, $Q\lfloor(u'_{pi})_{\mathrm{in},l}\rfloor$] along its trajectory. With this new information regarding each computational droplet, Eq. (16) has to be rewritten as

$$u_{pi} = \frac{\sum_{l=1}^{L}\sum_{m=1}^{M_l}\{n_{l,m}\cdot Q[(u'_{pi})_{\mathrm{in},l}]\}\cdot P[(u'_{gi})_m]\cdot(U_{pi})_m}{\sum_{l=1}^{L}\sum_{m=1}^{M_l}\{n_{l,m}\cdot Q[(u'_{pi})_{\mathrm{in},l}]\}\cdot P[(u'_{gi})_m]} \tag{18}$$

Here, L is the total count of issuing positions in the inlet station, and M_l is the subtotal count of the computational droplets for each discrete size, which are issued from the lth inlet position, entering the specified grid cell. Thus, with the measured data of $\overline{u'^2_{pi}}$ at the inlet stations that were provided in the experiments of Liu[11] and Hong,[13] the two-phase turbulent flow calculations considering the inlet u'_{pi} conditions can be performed with Eqs. (17) and (18).

In the computations of two-phase flows, the issue regarding to the grid resolution should be cared for in both the carrier and dispersed phases. The computational grid resolution can be generally improved using a finer grid mesh for the carrier phase. However, this inference cannot always work for the dispersed phase. First, the interfacial transport properties such as the drag coefficient are, in principle, derived from a single droplet surrounded by a uniform environment (u_{gi}, T_g, etc.), which is represented by the calculated carrier-phase properties in the specified grid cell. Consequently, there must be a restraint that the ratio of the grid size to the droplet size cannot be too small to meet this presumed boundary condition in deriving the interfacial transport properties. Another concern in choosing the grid size is to reduce the statistical shot noise in determination of the mean dispersed-phase properties through Eq. (16) or Eq. (18), or, more sensitively, through Eq. (19). With use of too fine a grid size, the statistical shot noise may become more remarkable. In consideration of 2% uncertainties in the velocity measurements made for the two test problems, a tradeoff between the grid resolution and the ratio of grid size to droplet size was made in the preceding studies[12,14] as follows. The area ratio (for the present two-dimensional problems) of the minimum grid cell to the largest droplet should be kept at least in $\mathcal{O}(10^2)$. Note that the governing equations are a parabolic type for the mixing layer flow and an elliptic type for the hollow-cone spray. For the mixing-layer problem, the marching step size is fixed with 1.5 mm (3% of the transverse width), whereas the transverse dimensions of the grid cells range from 0.5 mm (in the shear layer) to 1.5 mm (in the laterally outer freestream region). In contrast, a grid mesh constructed by 35×42 (axial by radial) is used for the calculations of the hollow-cone spray problem. The axial and radial dimensions of the grid cells range from 1.28 to 2.56 mm and from 1.28 to 3.20 mm, respectively.

IV. Results and Discussion

A. Planar Mixing Layer ($k_g > k_p$)

Although eight representative groups of droplets with various discrete sizes are used to simulate the spectral effects of the size distribution in the test problem. Only results with sizes of 10, 40, and 80 μm, representing small, medium, and large droplets, respectively, are reported here for the sake of brevity. Two predicted evolutions of the partial turbulent kinetic energy of the droplets, $(\overline{u'^2_p} + \overline{v'^2_p})/2$, of $d_p = 10$, 40, and 80 μm, with and without consideration of the inlet u'_{pi} conditions, are presented in Fig. 3 and are compared with the measured data of Liu.[11] Here, $\overline{u'^2_{pi}}$ is calculated from

$$\overline{u'^2_{pi}} = \frac{\sum_{m=1}^{M} n_m[(U_{pi})_m - u_{pi}]^2}{\sum_{m=1}^{M} n_m} \tag{19}$$

As revealed in our previous work,[9] at least 8000 computational droplets were required to obtain a statistically significant solution of the partial turbulent kinetic energy of the droplets by using the unsteady drag coefficient with inlet $u'_{pi} = 0$. However, the calculation with inlet u'_{pi} included, which leads to double levels of summation in determination of the mean values of the droplet velocities as described in Eq. (18), needs a relatively larger number (10,000) of the computation droplets to assure the statistically invariant solution. For the three selective droplet sizes of $d_p = 10$, 40, and 80 μm, each computational droplet represents 54, 25, and 1.1 real droplets, respectively, in the simulation with the use of as high a resolution

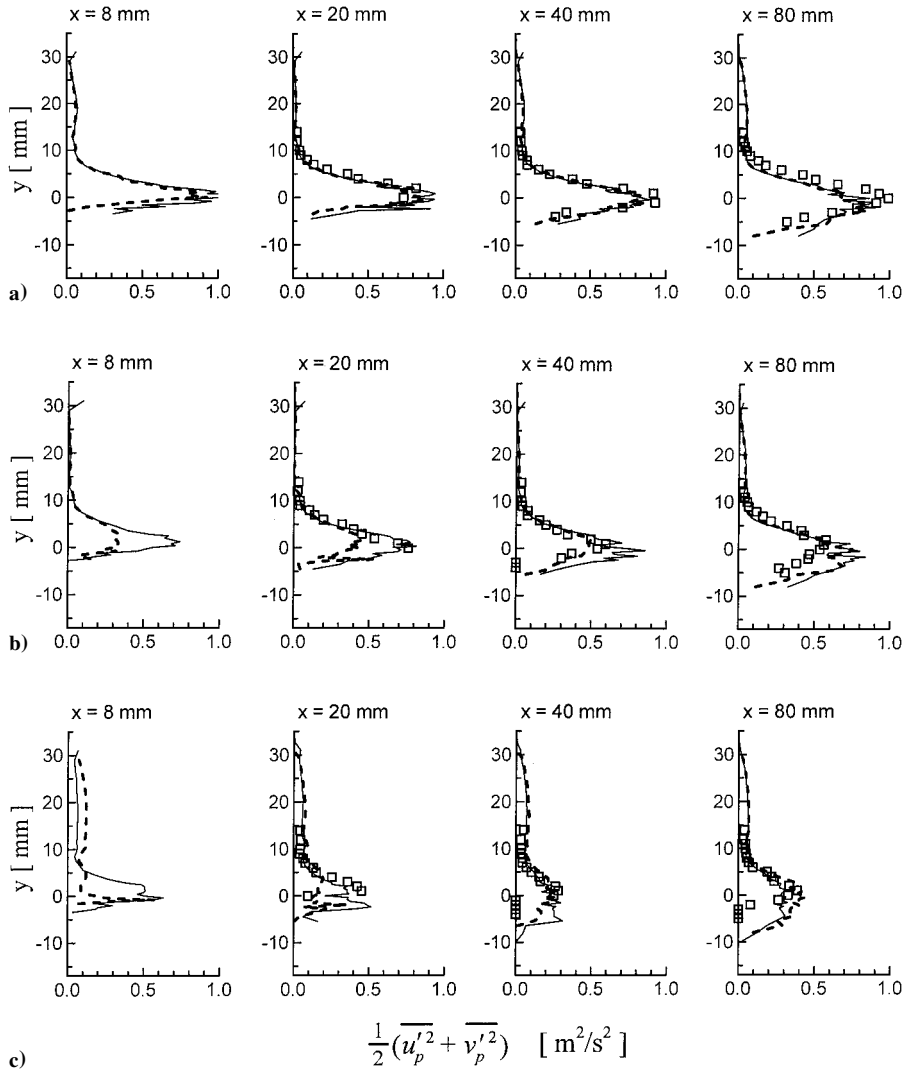

Fig. 3 Evolution of the two predicted, with and without consideration of inlet u'_{pi} conditions, and measured $(\overline{u_p'^2} + \overline{v_p'^2})/2$ of a) 10-, b) 40-, and c) 80-μm droplets in two-phase mixing layer: □, measurements[11]; ——, with inlet u'_{pi}; and - - - -, without inlet u'_{pi}.

as 10,000 computational droplets per discrete size. The predictions at the four streamwise stations, including a very upstream one ($x = 8$ mm) at which no measurements were made in the experiment of Liu,[11] are presented in Fig. 3 to explain the impact of the completeness of the employed inlet conditions on the solution of the fluctuating quantity of droplet velocity in the flowfield. Clearly, the calculation with inlet u'_{pi} included improves the prediction of the partial kinetic energy of droplets in the upstream regions, particularly as the droplet size is increased. It is agreed that small droplets such as $d_p = 10$ μm can reach their dynamic equilibrium with the carrier fluid more quickly than the larger droplets. As a result, the absence of the inlet u'_{pi} conditions in the stochastic Lagrangian calculation causes slight differences in the predictions of the partial kinetic energy of a droplet from those with inlet u'_{pi} included for the small droplet of $d_p = 10\mu$m, as shown in Fig. 3a.

Figure 2a reveals that the k_p values are much higher in the shear-layer region (around $y = 0$ mm) than in the freestream region. Therefore, the absence of the inlet u'_{pi} conditions should result in more prediction errors of the partial turbulent kinetic energy of droplets in the shear-layer region than in the freestream region, as shown in Fig. 3. From the mathematical point of view, the influence of the inlet conditions is appreciable in the initial region of the flowfield, and it becomes less significant in the downstream region. The deviations between the two predictions with inlet u'_{pi} included and with inlet $u'_{pi} = 0$, as observed in Fig. 3, are also consistent with this trend.

As pointed out before, because the influence of the inlet u'_{pi} conditions on the prediction of the partial kinetic energy of a droplet is more remarkable as the droplet size is increased, only the evolution of the mean streamwise and transverse velocity components of the largest droplet ($d_p = 80\,\mu$m), which are predicted with inlet u'_{pi} included, and with inlet $u'_{pi} = 0$, is presented in Fig. 4 for demonstration. Note that the velocity scales used in Figs. 4a and 4b are different. The differences in the predictions of mean droplet velocity between with inlet u'_{pi} included and with inlet $u'_{pi} = 0$ are much less appreciable than those of $(\overline{u_p'^2} + \overline{v_p'^2})/2$ as they appeared in Fig. 3c. The reason is as follows. The mean quantities of the dispersed phase are determined from the ensemble-averaging formulas, that is, Eq. (16) for the case with inlet $u'_{pi} = 0$ and Eq. (18) for the case with inlet u'_{pi} included, in which the only difference is the account of the inlet PDF value of u'_{pi} as one more weighting factor in Eq. (18). It is well understood that the larger the value of $(u'_{pi})_{\text{in}}$ sampled, the smaller the $Q\lfloor(u'_{pi})_{\text{in}}\rfloor$ value it is corresponding to, through Eq. (17). Accordingly, after a droplet leaves its inlet position, the resultant deviation of U_{pi}, which is determined from Eq. (1) with a sampled $(u'_{pi})_{\text{in}}$, from u_{pi} is evened out in the ensemble-averaging calculation of Eq. (18). Another observation made from Fig. 4 is that the consideration of inlet u'_{pi} conditions in the calculation permits the droplets to penetrate deeper to the low-speed stream side (lower part), which means a stronger turbulent dispersion effect can be numerically generated.

Because the test problem is a very dilute spray (the volumetric fraction of the droplets in the flow $<10^{-5}$) and the differences between the two u_{pi} predicted with inlet u'_{pi} included and with inlet $u'_{pi} = 0$ are slight even for the largest droplet (Fig. 4), the

Table 1 Ratio of the dynamic relaxation time to the residence time for 35-, 63-, and 119-μm droplets at locations $(x/D, r/D)$ of (50, 40) and (80, 60) for hollow-cone spray

$x/D, r/D$	U_g	U_p	$\lvert U_g - U_p \rvert$	Re_p	$\phi(Re_p)$	τ_r	τ_p	τ_p/τ_r
				35 μm				
(50,40)	1.17	6.64	5.4	12.6	1.913	3.8×10^{-4}	1.9×10^{-3}	5.19
(80,60)	0.88	2.08	1.2	2.8	1.298	1.2×10^{-4}	2.9×10^{-3}	2.36
				63 μm				
(50,40)	1.17	11.9	10.73	45.06	3.135	2.2×10^{-4}	3.9×10^{-3}	18.17
(80,60)	0.88	8.15	7.27	30.53	2.671	3.2×10^{-4}	4.5×10^{-3}	17.17
				119 μm				
(50,40)	1.17	13.9	12.73	100.9	4.551	1.8×10^{-4}	9.6×10^{-3}	53.3
(80,60)	0.88	11.2	10.32	81.8	4.111	2.3×10^{-4}	1.0×10^{-2}	46.6

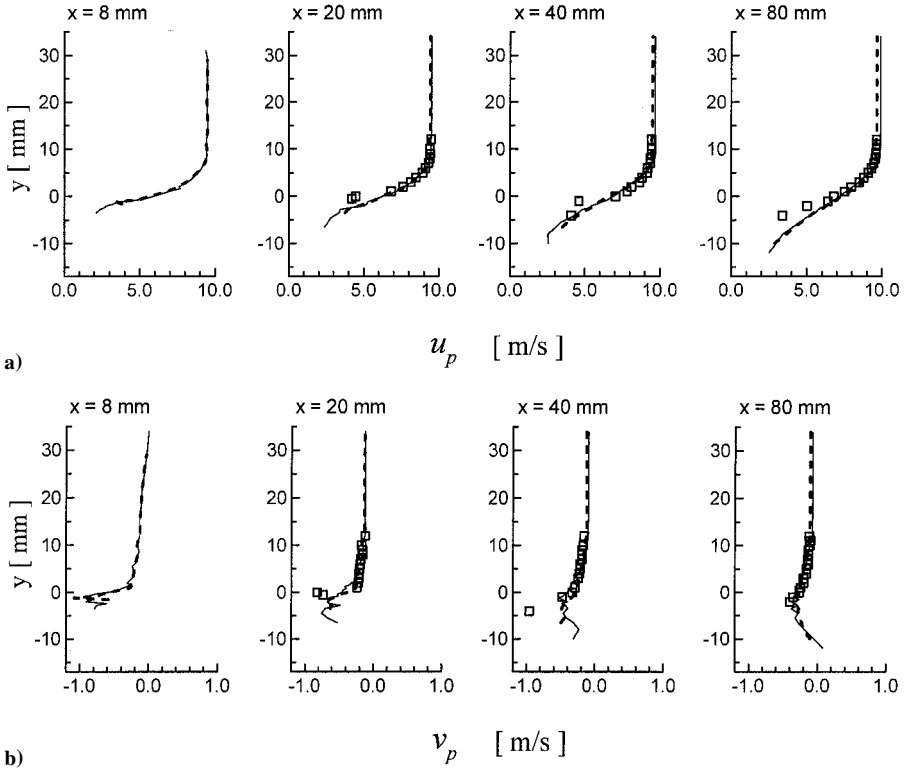

Fig. 4 Evolution of the two predicted, with and without consideration of inlet u'_{pi} conditions, and measured mean a) streamwise and b) transverse velocity components of 80-μm droplet in two-phase mixing layer: □, measurements[11]; ——, with inlet u'_{pi}; and - - - -, without inlet u'_{pi}.

carrier-phase solution (Eulerian part) is almost invariant in the present work. A detailed presentation and discussion on the carrier-phase flow properties is referred to in the work of Chang et al.[12] and is not repeated here.

B. Hollow-Cone Spray ($k_g < k_p$)

In the calculations to simulate the spectral distribution of the polydispersed spray for the second test problem, 10 representative groups of droplets with the discrete sizes ranging from 7 to 133 μm are used. It was pointed out by Chang et al.[14] that the occurrence of the secondary atomization process led to some peculiar velocity measurements for the droplets with small sizes. Because the present work does not account for the droplet breakup mechanism in the modeling, some deviations of the predictions, particularly for small droplets, from the measured data may occur. With this in mind, the three results with sizes of 35, 63, and 119 μm, representing small, medium, and large droplets, respectively, are reported here. Two test runs using 10,000 and 15,000 computational droplets for each discrete size are made with the unsteady drag coefficient and inlet u'_{pi} included. Note that the use of 15,000 computational droplets in the simulation is the highest resolution for the investigated spray because each computational droplet of the largest droplet ($d_p = 133$ μm) is almost equivalent to one real droplet. For the three selective droplet sizes of $d_p = 35$, 63, and 119 μm, each computational droplet now represents 77, 15, and 1.4 real droplets, respectively. Their predicted evolution of the partial kinetic energy of the droplets for three selective sizes are presented in Fig. 5 and compared with the measured data of Hong.[13] It is shown from Fig. 5 that even the use of as many as 15,000 computational droplets for each discrete size cannot effectively remove the statistical shot noise for large droplets such as the one with $d_p = 119$ μm. However, the differences between these two predictions of the partial kinetic energy of the droplets (Fig. 5c) are deemed mainly from the statistical shot noise. As discussed before, the u_{pi} values determined by the ensemble averaging of Eq. (18) are much less sensitive to the u'_{pi} deviations than the values of the partial kinetic energy of the droplets determined by Eq.(19). The following calculations are, therefore, made using 10,000 computational droplets for each discrete size.

In contrast to the first problem [i.e., droplet loading mixing layer, in which the typical magnitude orders of Re_p are in $\mathcal{O}(10^0 - 10^1)$], the typical magnitude orders of Reynolds number Re_p in the hollow-cone spray are in $\mathcal{O}(10^0 - 10^2)$ (Table 1). Note first the unsteady effect of the drag coefficient on the solution of the second problem. The quasisteady drag coefficient can be obtained from Eq. (7) by setting $K(t) = 0$. Note that the selective droplet of $d_p = 63$ μm is closer to the largest droplet size (80 μm) of the droplet loading

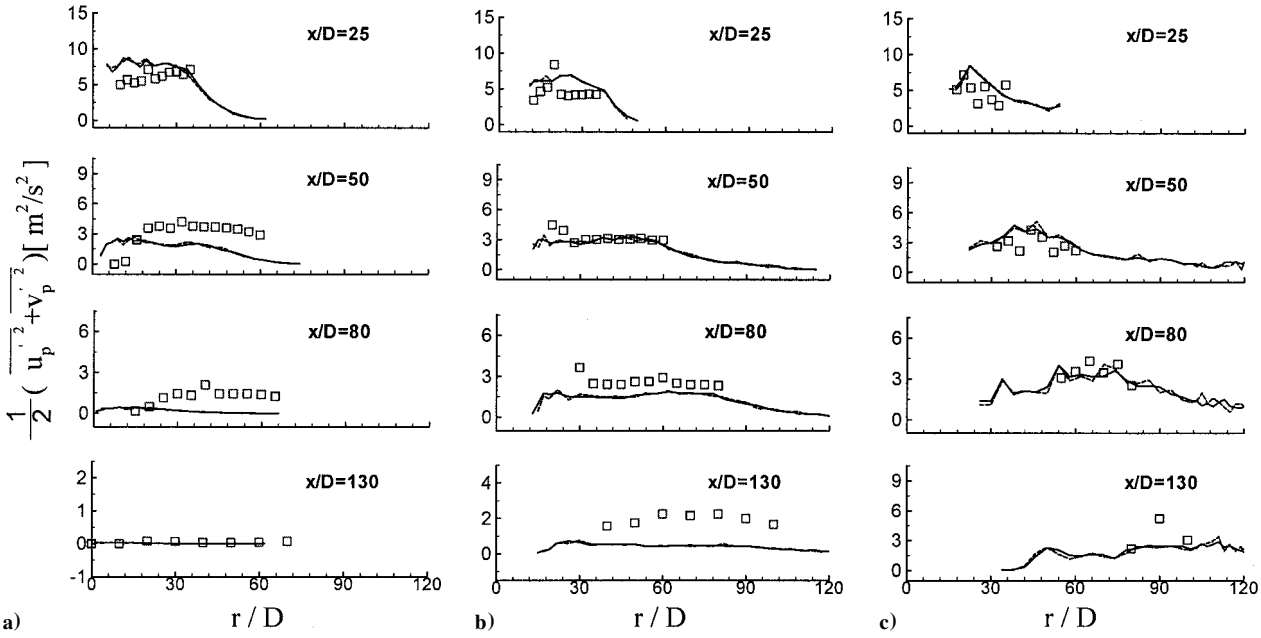

Fig. 5 Evolution of the two predicted, with 10,000 and 15,000 computational droplets for each discrete size, but all considering unsteady C_D and inlet u'_{pi}, and measured $(\overline{u'^2_p}+\overline{v'^2_p})/2$ of a) 35-, b) 63-, and c) 119-μm droplets in hollow-cone spray: □, measurements[13]; - - - -, 10,000 #/size; and ——, 15,000 #/size.

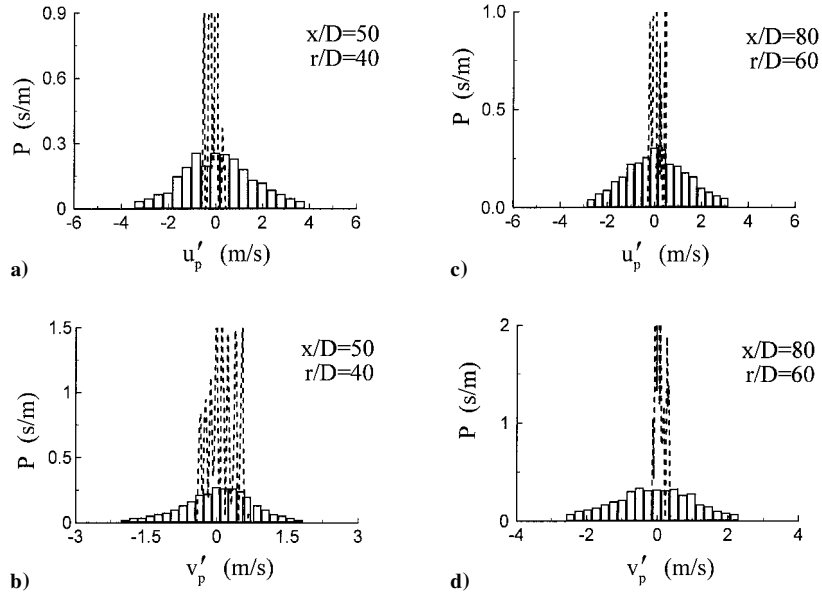

Fig. 6 Comparisons of predicted and measured PDFs of a) axial and b) radial fluctuating velocity components at position (50D, 40D) and of c) axial and d) radial fluctuating velocity components at position (80D, 60D) for 63-μm droplet by using quasisteady C_D, but with inlet $u'_{pi}=0$, in hollow-cone spray: |, measurements[13]; - - - -, without inlet (u'_{pi}) but with steady drag.

mixing layer in which its predicted PDFs of the velocity fluctuations can be effectively improved through use of the unsteady drag coefficient of Eq. (7) (Ref. 8). Thus, the PDF of the velocity fluctuations for the droplet with $d_p = 63$ μm is purposely presented here for demonstration. First, calculations are individually performed with the quasisteady and unsteady drag coefficients but all under the condition with inlet $u'_{pi}=0$. Their predicted PDFs of the axial and radial fluctuating velocity components at two positions, (50D, 40D) and (80D, 60D), are displayed in Figs. 6 and 7 and compared with the measured data.[13] Here the predicted PDF indicates the u'_{pi} distribution of the collected number of the computational droplets traveling through the cell of a specified grid node. Clearly, the consideration of the unsteady drag coefficient cannot improve the PDF shape as performed in the two-phase mixing layer.[9] A further analysis for the preceding observation is as follows. By setting $K(t)=0$ (quasisteady) in Eq. (7) and substituting it into Eq. (2), it yields

$$\tau_p = \frac{\rho_p (d_p)^2}{18\mu_g}\frac{1}{\phi(Re_p)} \tag{20}$$

As mentioned before, the typical values of Reynolds number Re_p in this test problem are $\mathcal{O}(10^0-10^2)$ which are generally one order of magnitude larger than those in the preceding two-phase mixing layer problem. The definition of Reynolds number Re_p, Eq. (9), shows that Reynolds number Re_p is proportional to the droplet size. Equation (12) indicates that $\phi(Re_p)$ becomes larger as Reynolds number Re_p is increased, which in turn makes τ_p smaller as shown

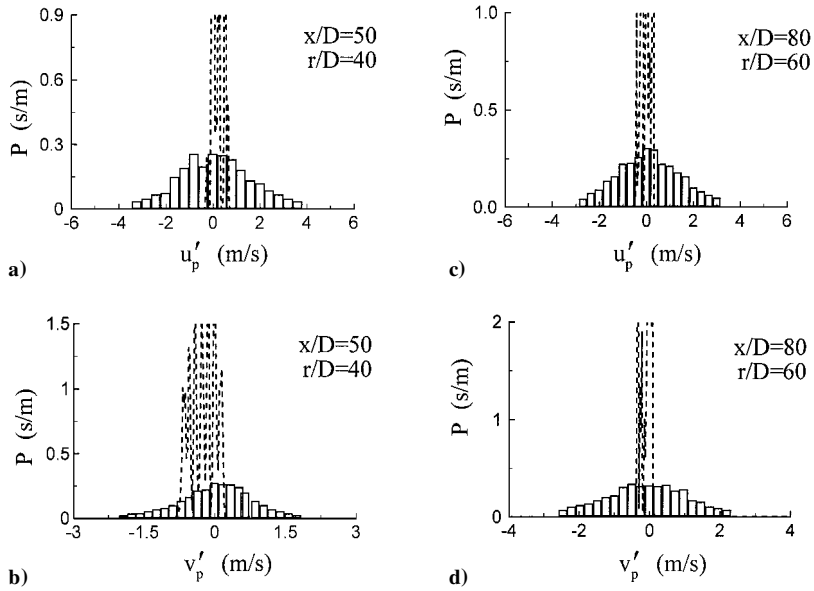

Fig. 7 Comparisons of predicted and measured PDFs of a) axial and b) radial fluctuating velocity components at position (50*D*, 40*D*) and of c) axial and d) radial fluctuating velocity components at position (80*D*, 60*D*) for of 63-μm droplet by using unsteady C_D, but with the inlet $u'_{pi} = 0$, in hollow-cone spray: |, measurements[13]; - - - -, without inlet (u'_{pi}) but with unsteady drag.

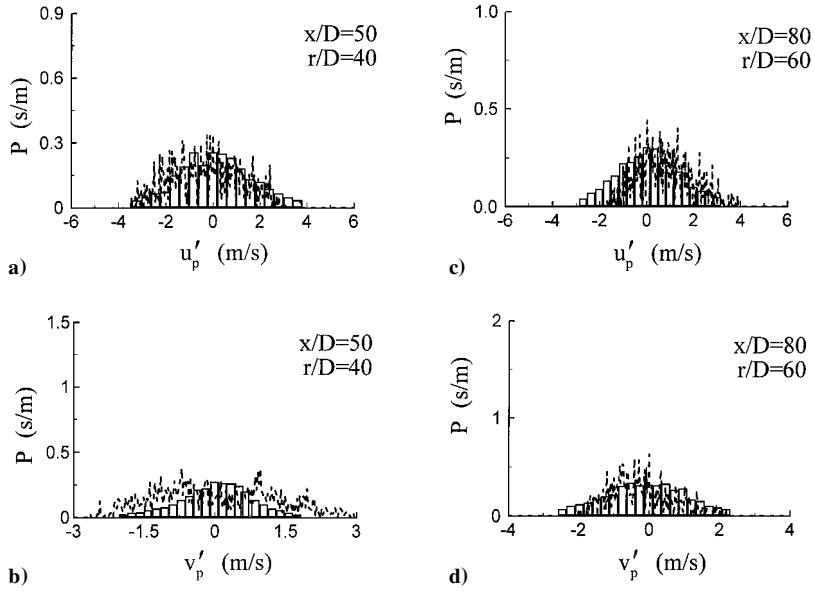

Fig. 8 Comparisons of predicted and measured PDFs of a) axial and b) radial fluctuating velocity components at position (50*D*, 40*D*) and of c) axial and d) radial fluctuating velocity components at position (80*D*, 60*D*) for 63-μm droplet by using quasisteady C_D, but with inlet u'_{pi}, included in hollow-cone spray: |, measurements[13]; - - - -, with inlet (u'_{pi}) and steady drag.

in Eq. (20). This trend can be clearly seen in Table 1. In contrast, the residence times τ_r shown in Table 1 do not exhibit this size-dependent trend, but all remain randomly in the range between 1.2×10^{-4} and 3.8×10^{-4} s for the droplet sizes changing from 35 to 119 μm. Table 1 also summarizes the Stokes numbers defined by

$$\mathrm{St} = \tau_p/\tau_r \tag{21}$$

at these two positions for the three selective droplet sizes. Note that the Stokes number values for $d_p = 63$ μm are only in $\mathcal{O}(10^1)$, whereas those for $d_p = 119$ μm are in $\mathcal{O}(10^2)$, which is the same order of magnitude for the largest droplet ($d_p = 80$ μm) in the two-phase mixing layer.[9] This issue will be elaborated on later.

Calculations are redone, but now under the condition with inlet u'_{pi} included. The predicted PDFs, using the quasisteady drag coefficient, at the two positions are displayed in Fig. 8. Clearly, the predicted PDF shapes are significantly improved by accounting for the inlet u'_{pi} conditions, even using the quasi-steady drag coefficient. The predicted PDF shapes obtained with considerations of unsteady drag coefficient and inlet u'_{pi} conditions look like Fig. 8 and are not presented here for the sake of brevity. In contrast to only u'_{pi} information at the two points of the flowfield given in Figs. 6–8, Fig. 9 presents the evolution of the partial kinetic energy of the droplets with three selective sizes predicted with the unsteady and quasi-steady drag coefficients under the consideration of inlet u'_{pi} included or inlet $u'_{pi} = 0$, in comparison with the measured data of Hong.[13] Note that, to discern the difference between the predictions,

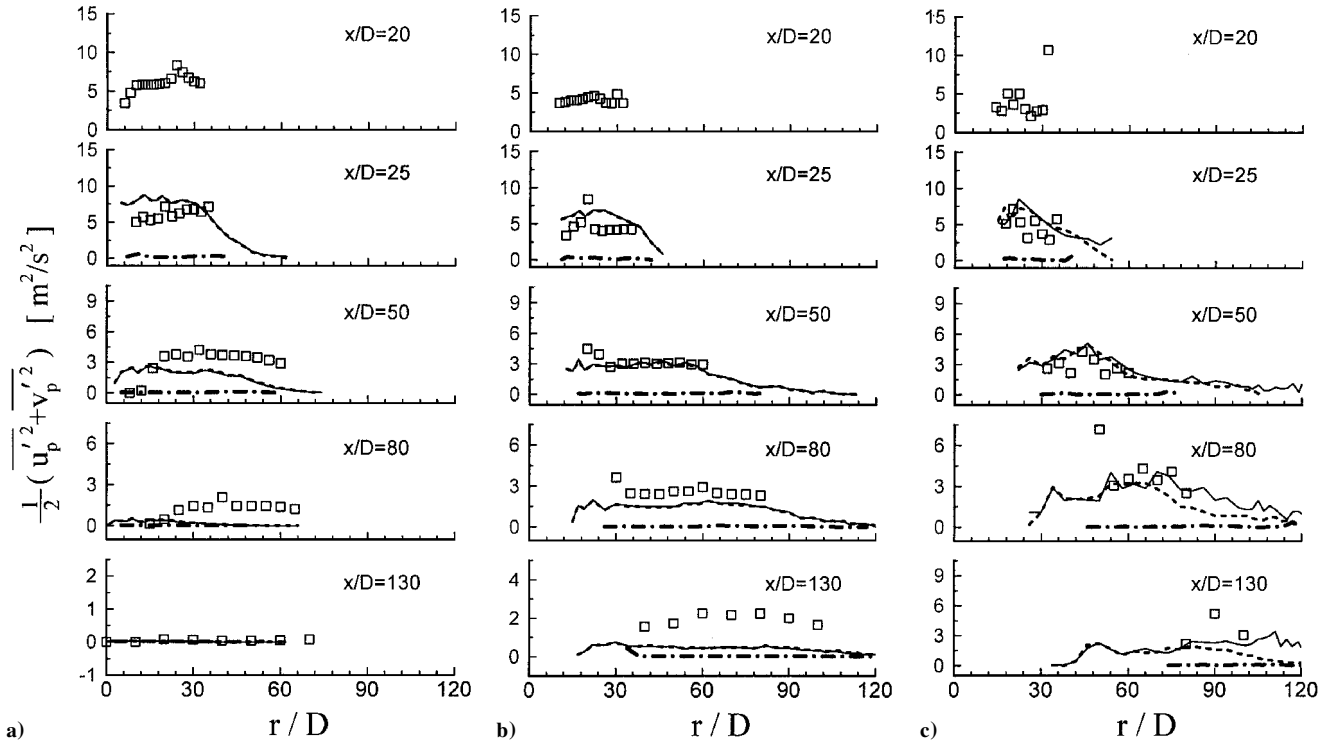

Fig. 9 Evolution of the three predicted, by using the unsteady or quasisteady drag coefficient under consideration, with or without the inlet u'_{pi} conditions, and measured $(u'^2_{pi}+v'^2_{pi})/2$ of a) 35-, b) 63-, and c) 119-μm droplets in hollow-cone spray: □, measurements[13]; ——, with inlet (u'_{pi}) and unsteady drag; -·-·-, without inlet (u'_{pi}) but with unsteady drag; and - - - -, with inlet (u'_{pi}) and steady drag.

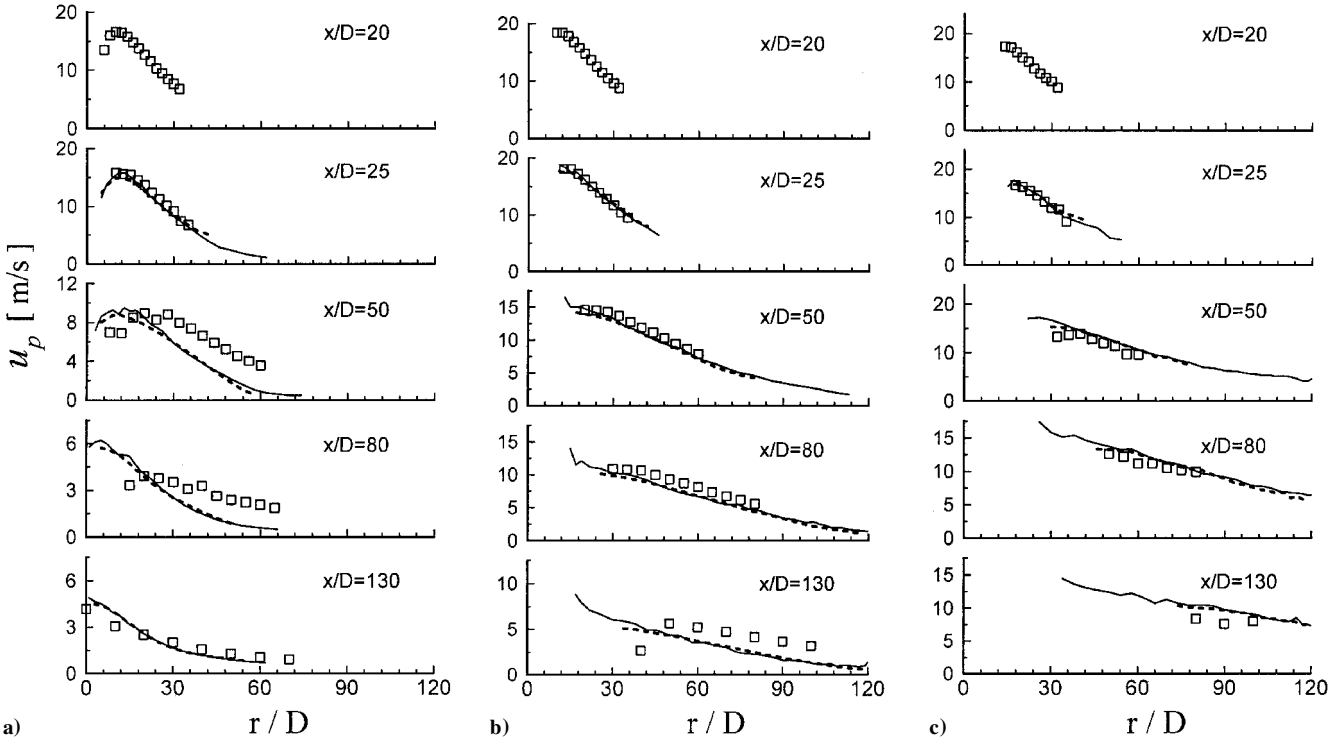

Fig. 10 Evolution of the two predicted, with and without considering inlet u'_{pi} conditions, but all using the unsteady C_D, and measured mean axial velocity component of a) 35-, b) 63-, and c) 119-μm droplets in hollow-cone spray: □, measurements[13]; ——, with inlet (u'_{pi}); and - - - -, without inlet (u'_{pi}).

the scales in the ordinates of Figs. 9–12 have been purposely enlarged in some downstream axial stations. It is clearly shown in Fig. 9 that the partial kinetic energy of the droplets are significantly underpredicted in the case with inlet $u'_{pi}=0$, even though the unsteady C_D is used. The differences in the predictions between using the unsteady and quasisteady drag coefficients, as shown in Fig. 9, become more remarkable when the St values reach $\mathcal{O}(10^2)$, as revealed in Table 1.

Figures 10 and 11 present the evolution of the two predicted, with inlet u'_{pi} included and with inlet $u'_{pi}=0$, but all using the unsteady C_D, and measured mean axial and radial velocity components, respectively, of the droplets with these three selective sizes. Again, the ensemble-averaging formula weighted with the PDF value of inlet u'_{pi} smears out, to a great extent, the very remarkable differences of U_{pi} predictions as implied from Fig. 9. Nevertheless, more, wider turbulent dispersion regions for the all-size droplets can be obtained

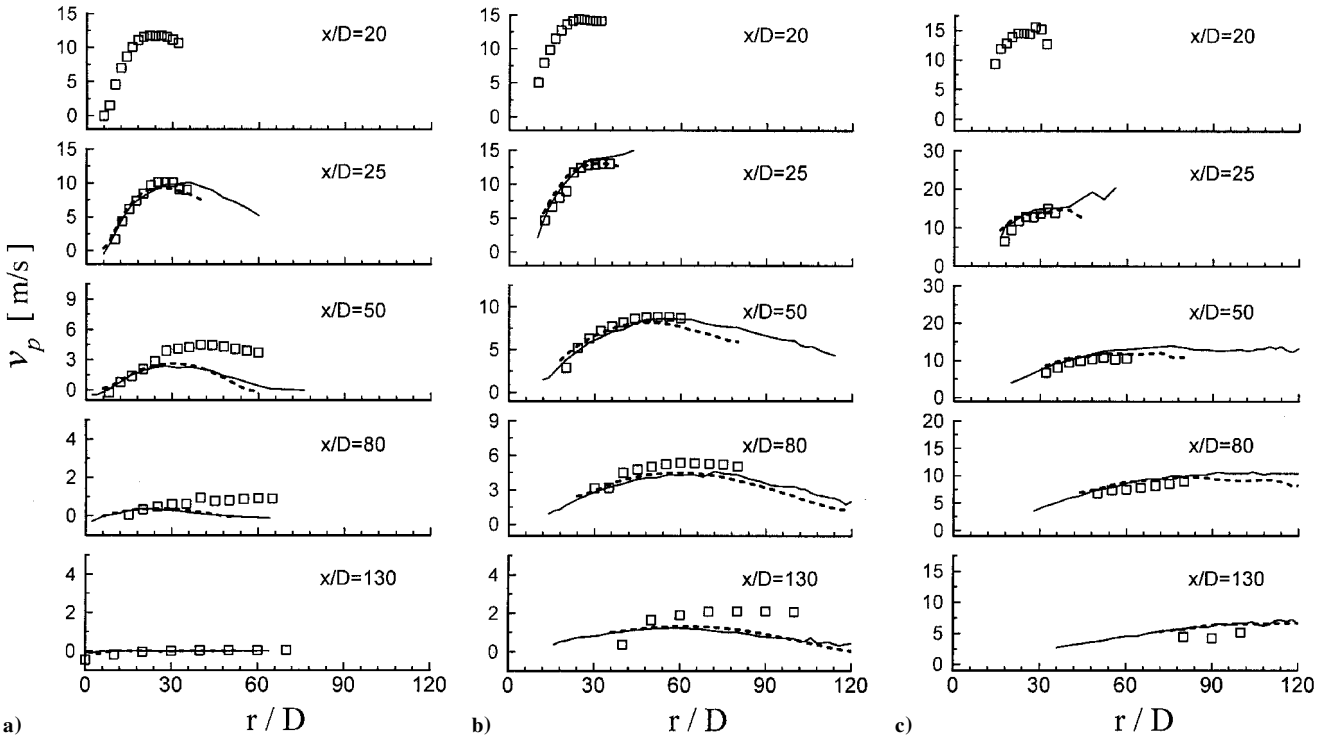

Fig. 11 Evolution of the two predicted, with and without considering inlet u'_{pi} conditions, but all using the unsteady C_D, and measured mean radial velocity component of a) 35-, b) 63-, and c) 119-μm droplets in hollow-cone spray: □, measurements[13]; ——, with inlet (u'_{pi}); and - - - -, without inlet (u'_{pi}).

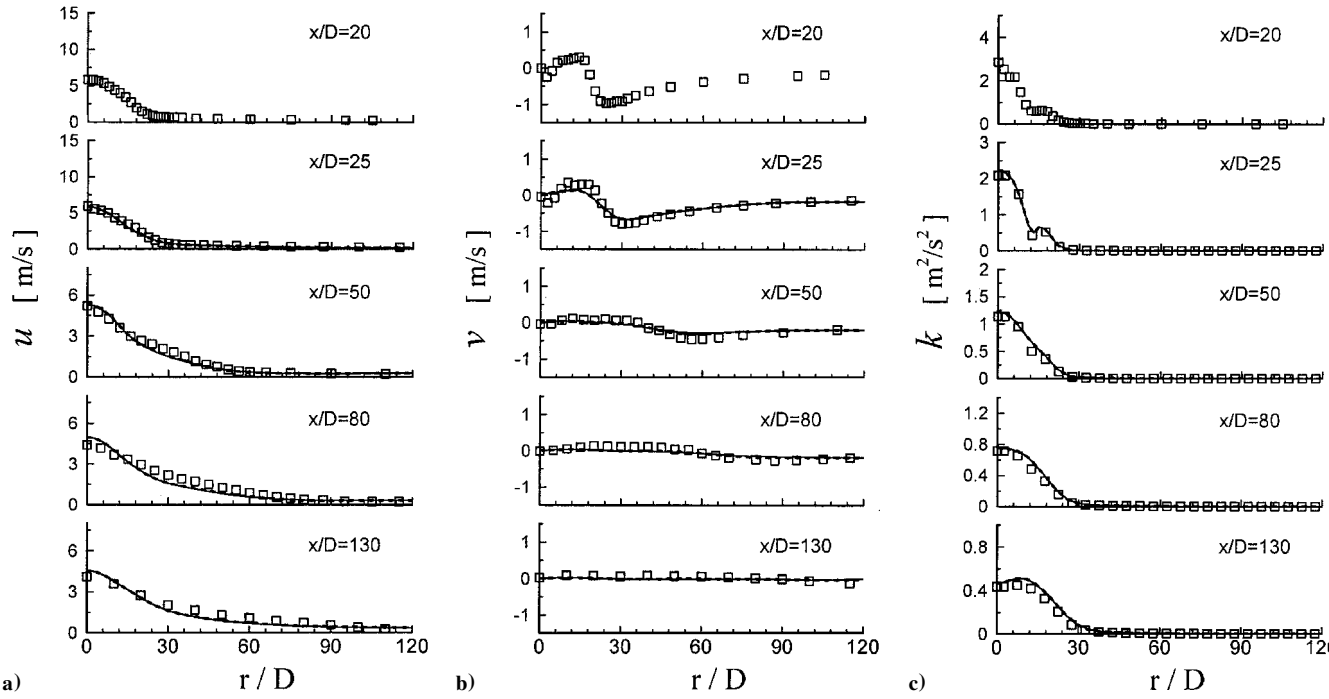

Fig. 12 Evolution of the two predicted, with and without considering inlet u'_{pi} conditions, but all using the unsteady C_D, and measured a) mean axial velocity component, b) mean radial component, and c) turbulent kinetic energy of carrier fluid in hollow-cone spray: □, measurements[13]; ——, with inlet (u'_{pi}); and - - - -, without inlet (u'_{pi}).

in the case with inlet u'_{pi} included than that with inlet $u'_{pi} = 0$. In other words, neglect of the inlet u'_{pi} conditions in the calculation leads to remarkable underpredictions of the turbulent dispersion ability of the droplets for the present test problem in which k_p is much larger than k_g at the inlet, as shown in Fig. 2.

As mentioned in Sec. III, the hollow-cone spray is a relatively denser two-phase flow than the droplet loading mixing layer. The evolution of the two predicted, with inlet u'_{pi} included and with inlet $u'_{pi} = 0$, but all using the unsteady C_D, and measured mean axial and radial velocity components, as well as turbulent kinetic energy of the carrier phase, is presented in Fig. 12. Clearly, no remarkable differences between these two predictions can be observed due to the diluteness [the volumetric fractions of the droplets are at most $\mathcal{O}(10^{-4})$] of the test problem. However, the excellent agreements between the predictions and measurements confirm the applicability of the employed physical model and numerical method in this work.

A comparison of Fig. 9a (the partial turbulent kinetic energy of the droplet with $d_p = 35\ \mu$m) and Fig. 12c (the turbulent kinetic energy of the carrier fluid) shows that the velocity fluctuations of the small droplets decay faster and that $k_p < k_g$ when the small droplets reaching the downstream axial station of $x/D = 30$. In contrast, the partial turbulent kinetic energy of the larger droplets, such as $d_p = 63$ and $119\ \mu$m, are still higher than k_g even at this far downstream axial station. A comparison made between Figs. 9a and 12c also corroborates the inference for the occurrence of the secondary atomization process made by Chang et al.,[14] that is, the much higher measured data of $(\overline{u_p'^2} + \overline{v_p'^2})/2$ shown in the axial stations of $x/D = 50$ and 80 in Fig. 9a were associated with the droplets, broken up from the larger droplets, which possessed larger partial turbulent kinetic energy as revealed in Figs. 9b and 9c. Further discussion on this issue can be found in Ref. 14.

V. Conclusions

The effect of the inlet u'_{pi} conditions on the solution of the two-phase turbulent flow, which is solved with the stochastic Lagrangian method, is examined through the two representative, well-defined problems. One is the droplet loading, planar mixing layer which is associated with $k_g > k_p$ at the inlet, and the other is a practical hollow-cone spray in which k_g is much less than k_p at the distance just after the primary atomization process. The study shows that the inlet u'_{pi} conditions have to be considered in the calculations to obtain complete, correct solution of the dispersed-phase turbulence characteristics, in particular for the two-phase flows possessing $k_g < k_p$. The study also concludes that the unsteady drag coefficient has to be considered in the model formulation when the local Stokes number values larger than $\mathcal{O}(10^1)$ are encountered in the examined two-phase turbulent flowfield. The price to be paid by accounting for the inlet u'_{pi} conditions and the unsteady drag coefficient in the calculation is that a great number of $\mathcal{O}(10^4)$ of the computational droplets for each discrete size is required in comparison with the number of $\mathcal{O}(10^3)$ of the computational droplets for each discrete size, which was previously suggested by Chang and Wu[6] to obtain the statistically invariant solution, in association with quasisteady drag coefficient and inlet $u'_{pi} = 0$, of the mean flow properties only.

Acknowledgment

The authors gratefully acknowledge support from the National Science Council of the Republic of China under Grant NSC89-2212-E006-129.

References

[1]Gosman, A. D., and Ioannides, E., "Aspects of Computer Simulation Liquid-Fueled Combustors," AIAA Paper 81-0323, June 1981.

[2]Crowe, C. T., Troutt, T. R., and Chung, J. N., "Numerical Models for Two-Phase Turbulent Flow," *Annual Review of Fluid Mechanics*, Vol. 28, No. 1, 1996, pp. 11–43.

[3]Shirolkar, J. S., Coimbra, C. F. M., and Queiroz McQuay, M., "Fundamental Aspects of Modeling Turbulent Particle Dispersion in Dilute Flow," *Progress in Energy and Combustion Science*, Vol. 22, No. 4, 1996, pp. 363–399.

[4]Sirignano, W. A., "Fluid Dynamics of Sprays—1992 Freeman Scholar Lecture," *Journal of Fluids Engineering*, Vol. 115, No. 3, 1993, pp. 345–378.

[5]Chen, X. Q., and Pereira, J. C. F., "Stochastic-Probabilistic Efficiency Enhanced Dispersion Modeling of Turbulent Polydispersed Sprays," *Journal of Propulsion and Power*, Vol. 12, No. 4, 1996, pp. 760–769.

[6]Chang, K. C., and Wu, W. J., "Sensitivity Study on Monte Carlo Solution Procedure of Two-Phase Turbulent Flow," *Numerical Heat Transfer*, Pt. B, Vol. 25, No. 2, 1994, pp. 223–244.

[7]Dutta, P., Sivathanu, Y. R., and Gore, J. P., "Discrete Probability Function Method for the Calculation of Turbulent Particle Dispersion," *AIAA Journal*, Vol. 35, No. 1, 1997, pp. 200–202.

[8]Chen, X. Q., and Pereira, J. C. F., "Computation of Particle-Laden Turbulent Gas Flows Using Two Dispersion Models," *AIAA Journal*, Vol. 36, No. 4, 1998, pp. 539–546.

[9]Chang, K. C., and Yang, J. C., "Unsteady Drag Consideration in Stochastic Eulerian–Lagrangian Formulation of Two-Phase Flow," *AIAA Journal*, Vol. 37, No. 4, 1999, pp. 434–442.

[10]Chang, K. C., Wu, W. J., and Wang, M. R., "Limitations of the Stochastic Approach in Two-Phase Turbulent Flow Calculations," *Atomization and Sprays*, Vol. 6, No. 2, 1996, pp. 211–225.

[11]Liu, Y. C., "Transition of the Planar Mixing Layer Under Particle Loading," Ph.D. Dissertation, Dept. of Aeronautics and Astronautics, National Cheng-Kung Univ., Tainan, Taiwan, ROC, Dec. 1991.

[12]Chang, K. C., Wang, M. R., Wu, W. J., and Liu, Y. C., "Theoretical and Experimental Study on Two-Phase Structure of Planar Mixing Layer," *AIAA Journal*, Vol. 31, No. 1, 1993, pp. 68–74.

[13]Hong, C. H., "Dynamic Characteristics of the Continuous and Dispersed Phase in a Hollow-Cone Spray," Ph.D. Dissertation, Dept. of Aeronautics and Astronautics, National Cheng-Kung Univ., Tainan, Taiwan, ROC, Nov. 1991.

[14]Chang, K. C., Wang, M. R., Wu, W. J., and Hong, C. H., "Experimental and Theoretical Study on Hollow-Cone Spray," *Journal of Propulsion and Power*, Vol. 9, No. 1, 1993, pp. 28–34.

[15]Prevost, F., Boree, J., Nuglisch, H. J., and Charnay, G., "Measurements of Fluid/Particle Correlated Motion in the Far Field of an Axisymmetric Jet," *International Journal of Multiphase Flow*, Vol. 22, No. 4, 1996, pp. 685–701.

[16]Shuen, J. S., Solomon, A. S. P., Zhang, Q. F., and Faeth, G. M., "A Theoretical and Experimental Study of Turbulent Particle-Laden Jets," NASA CR-1682-93, 1983.

[17]Shuen, J. S., Solomon, A. S. P., Zhang, Q. F., and Faeth, G. M., "Structure of Particle-Laden Jets: Measurements and Predictions," *AIAA Journal*, Vol. 23, No. 3, 1985, pp. 396–404.

[18]Shang, H. M., Chen, C. P., and Jiang, Y., "Turbulence Modulation Effect on Evaporating Spray Characterization," AIAA Paper 90-2442, 1990.

[19]Mei, R., and Adrian, R. J., "Flow Past a Sphere with an Oscillation in the Free-Stream and Unsteady Drag at Finite Reynolds Number," *Journal of Fluid Mechanics*, Vol. 237, April 1992, pp. 323–341.

[20]Clift, R., Grace, J. R., and Weber, M. E., *Bubbles, Drops and Particles*, Academic Press, New York, 1978, Chap. 5.

[21]Sano, T., "Unsteady Flow Past a Sphere at Low Reynolds Number," *Journal of Fluid Mechanics*, Vol. 112, Nov. 1981, pp. 433–441.

[22]Patankar, S. V., *Numerical Heat Transfer and Fluid Flow*, McGraw–Hill, New York, 1980, Chap. 6.

J. P. Gore
Associate Editor